

Snapshots of nuclear pore complexes in action captured by cryo-electron tomography

Martin Beck¹, Vladan Lučić¹, Friedrich Förster¹, Wolfgang Baumeister¹ & Ohad Medalia^{1†}

Nuclear pore complexes reside in the nuclear envelope of eukaryotic cells and mediate the nucleocytoplasmic exchange of macromolecules¹. Traffic is regulated by mobile transport receptors that target their cargo to the central translocation channel, where phenylalanine-glycine-rich repeats serve as binding sites². The structural analysis of the nuclear pore is a formidable challenge given its size, its location in a membranous environment and its dynamic nature. Here we have used cryo-electron tomography³ to study the structure of nuclear pore complexes in their functional environment, that is, in intact nuclei of *Dictyostelium discoideum*. A new image-processing strategy compensating for deviations of the asymmetric units (protomers) from a perfect eight-fold symmetry enabled us to refine the structure and to identify new features. Furthermore, the superposition of a large number of tomograms taken in the presence of cargo, which was rendered visible by gold nanoparticles, has yielded a map outlining the trajectories of import cargo. Finally, we have performed single-molecule Monte Carlo simulations of nuclear import to interpret the experimentally observed cargo distribution in the light of existing models for nuclear import.

A variety of electron microscopy approaches has been used to elucidate the overall architecture of nuclear pore complexes (NPCs)¹ but substantial improvements in resolution are needed to use three-dimensional electron microscopy maps as a frame into which high-resolution structures of individual nucleoporins or of larger modules can be fitted with confidence. Hitherto, most electron microscopy studies used preparations derived from isolated nuclear envelopes, often by detergent extraction, which bears the risk of artefacts such as the loss of components, and it compromises our ability to perform studies under physiologically relevant conditions. Cryo-electron tomography is an imaging modality that combines the potential of three-dimensional imaging with a close-to-life preservation of biological samples, and it allows the investigation of large structures with unique topologies (such as organelles or even whole cells) at molecular resolution³. We have shown previously that cryo-electron tomography can be applied to intact, transport-competent nuclei from *Dictyostelium discoideum*, providing new insights into the structure and dynamics of the NPC⁴.

It had been noted before that NPCs exhibit plasticity⁵ and show conspicuous deviations from eight-fold symmetry to the extent that supernumerary protomers are incorporated into the complex⁶. To avoid the fact that deviations from rotational symmetry limit resolution, we used an image-processing strategy akin to the correlation averaging or unbending of distorted lattices⁷. An initial reference was created by averaging tomograms of 523 NPCs with an imposed eight-fold symmetry; from this average, a segment was cut out comprising one complete protomer flanked by two half protomers. This reference was then used in a refinement cycle. After mapping 4,184

asymmetric units individually and aligning them, a new average was created. The improvement in resolution that can be achieved depends on the accuracy with which individual protomers can be located and on their mode of accommodating distortions (non-rigid compared with rigid body movements)⁸. The significant improvement in resolution that we obtained (from 8.3 nm to 5.8 nm; Supplementary Fig. 3) indicates that individual protomers can indeed be located with sufficient accuracy. The measured displacement of the protomers (4.6 nm mean in-plane displacement from symmetry-related positions) is consistent with these values (Fig. 1a, b). Out-of-plane displacements of the protomers seem to be negligible. Most NPCs assume a slightly elliptical shape that entails a small change of the pore diameter as compared to a perfectly symmetric ring structure (Fig. 1c, d). Notably, a recent structural study of Nup58/45 indicates that the diameter of the central transport channel is adjusted by circumferential sliding of this subcomplex⁹. The refined component averages were reassembled computationally into a complete model of the NPC (see below); in an animated representation, the measured distortions were translated into motions (see Supplementary Movie 1).

With the improvement in resolution, several new features were revealed: the cytoplasmic ring, spoke ring and nuclear ring are now seen as distinct but nevertheless connected structures (Fig. 2a, b). In contrast to the nuclear ring, the cytoplasmic ring seems to be only weakly connected to the spoke ring. The spokes form a ring with an inner diameter of 75 nm, whereas the fused inner nuclear membrane and outer nuclear membrane form a ring of 105 nm in diameter. A cut-away view of a protomer (Fig. 2c) shows the interactions of the three rings with the membrane. Each spoke has a clamp-like shape and is attached to the membrane at two specific sites. The spoke ring apparently stabilizes the membrane curvature, a task previously ascribed to the Nup107 subcomplex¹⁰. Interestingly, Nup133, a member of this subcomplex, contains an amphipathic α -helical motif for sensing membrane curvature¹¹. The contact region between the membrane and the spoke ring is a porous, sponge-like structure. In a three-dimensional surface-rendered view, it seems to be traversed by a channel of approximately 9 nm in diameter (Fig. 2c and Supplementary Fig. 2a). It has been suggested previously that an alternative passageway exists that is used exclusively by small molecules, allowing them to bypass the meshwork of phenylalanine-glycine repeats residing in the central channel¹². We have not found evidence suggesting that classical import cargo can be transported through these regions (see below). However, recent observations¹³ suggest that import of inner nuclear membrane proteins proceeds along a path near the NPC adjacent to the membrane.

A striking feature is the existence of a luminal connector element spanning the space between the inner nuclear membrane and outer nuclear membrane near the periphery of the NPC (Fig. 2c, e). It is

¹Max Planck Institute of Biochemistry, D-82152 Martinsried, Germany. [†]Present address: The Department of Life Sciences, The Ben Gurion University and the NIBN, Beer Sheva 84105, Israel.

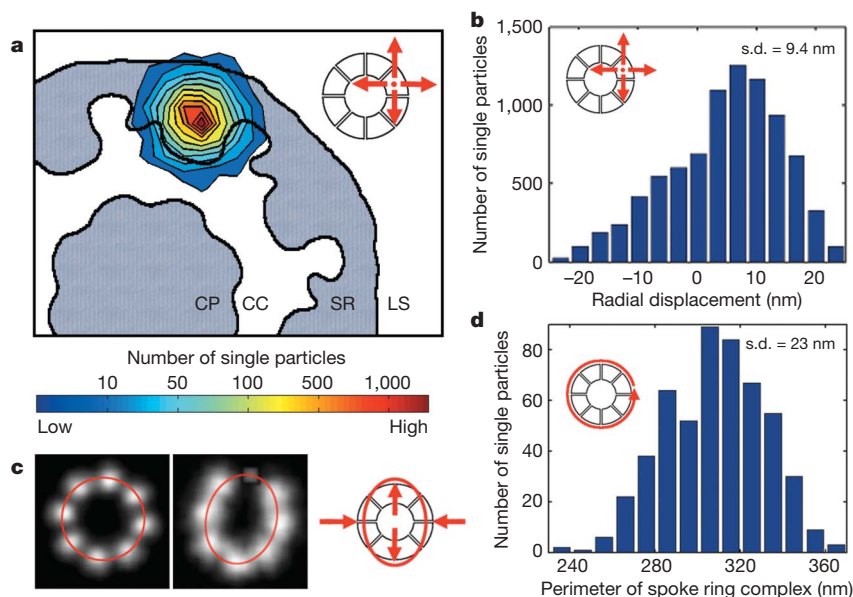


Figure 1 | Plasticity of intact NPCs is revealed by displacement analysis. **a**, Heat map showing the displacement of a NPC asymmetric unit (protomer) from the ideal eight-fold rotational symmetric arrangement within the spoke ring plane (superimposed). CC, central channel; CP, central plug; LS, luminal space; SR, spoke ring. **b**, Distribution of the radial displacement of the asymmetric units (mean 4.6 nm, s.d. 9.4 nm). **c**, Elliptical distortions of individual NPCs visualized as the probability density of the

positions of the eight protomers (white). Left: when eight-fold rotational symmetry is imposed, the positions of the protomers form a circle (red). Right: protomer positions form an ellipse (red) when the alignment is performed with individual NPCs. The subunits located at one end of their major (long) axes were used as reference points for the alignment (see the top protomer on the figure). **d**, Distribution of the perimeter of the spoke ring complex of individual NPCs.

attached to the membrane at the opposite sides of the membrane contacts of the cytoplasmic and nuclear rings, correspondingly. In view of the otherwise frail contacts, this connector may be a key

element in the stabilization of the whole structure. It might define the distance of 30 nm between the inner nuclear membrane and outer nuclear membrane and contribute to the maintenance of the

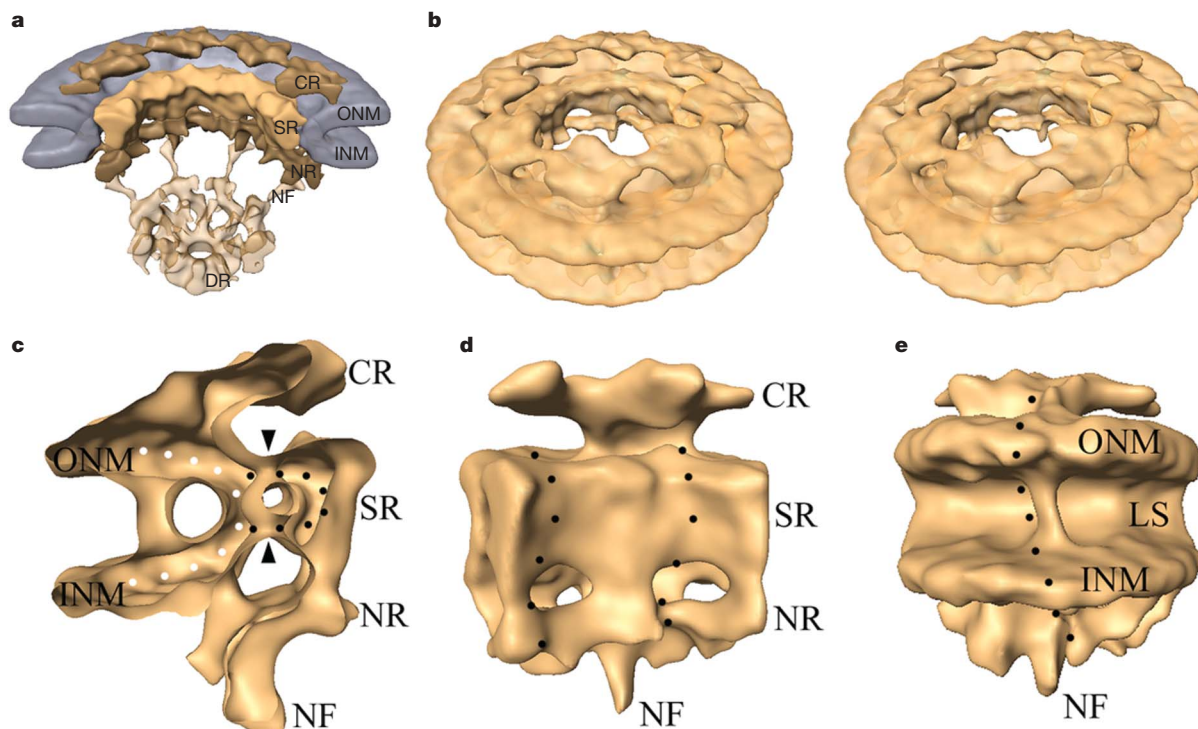


Figure 2 | Refined structure of the *Dictyostelium* NPC. **a**, Cut-away view of the structure of rejoined asymmetric units with subjective segmentation for the cytoplasmic (CR), spoke (SR) and nuclear rings (NR) in shades of yellow, and the inner (INM) and outer nuclear membrane (ONM) in bluish-grey. For clarity, the CP/T has been omitted and the basket with nuclear filaments (NF) and distal ring (DR) was rendered transparent. **b**, Stereo view of the scaffold structure of the NPC. **c**, Cut-away view of a protomer. The fused

inner nuclear membrane and outer nuclear membrane and the clamp-shaped spoke structure are indicated by white dots and black dots, respectively; arrowheads mark the entry and exit of an apparent channel. **d**, Averaged structure of a protomer flanked by two half protomers seen from the central channel (black dots mark the protomer boundaries). **e**, View from the luminal space (LS). Black dots follow the rod-shaped structure that connects the cytoplasmic and nuclear rings.

membrane curvature. In contrast to earlier studies with *Xenopus* NPCs⁵, the luminal structure observed with *Dictyostelium* NPCs is not ring-shaped but rod-shaped. The largest outer diameter of the entire NPC (135 nm) is defined by this membrane-spanning element.

Although tomography is normally a static tool, it can be used to take snapshots of processes, and, if these are properly superimposed, allows one to deduce the course of dynamic events: in this case, tomography has been used to visualize the trajectories of cargo as it traverses the NPC. To map the routes taken by cargo, we mapped the positions of a gold-labelled fusion protein consisting of a nuclear localization signal and two copies of green fluorescent protein (NLS-2×GFP) during translocation. This model substrate for the classical import pathway has been well characterized¹⁴. We determined the positions of 638 cargo molecules within 251 labelled NPCs and used the experimentally determined coordinates of individual gold-labelled cargoes to compute a three-dimensional probability density map of classical import cargo at the nuclear pore complex (Fig. 3 and Supplementary Fig. 4). The central plug or transporter (CP/T) is an electron-dense structure within the central channel that seems to be tripartite on the level of the cytoplasmic, spoke and nuclear rings, respectively⁴. The observed locations of cargo and the probability map derived from them match the shape of the CP/T electron microscopy density well, confirming that the mass observed within the central channel can at least partially be ascribed to cargo, as suggested previously². However, the cargo

density was relatively low in a region with a maximum diameter of 20 nm in the middle of the central channel (in plane with the spoke ring). Notably, the corresponding region of the CP/T exhibits a high electron microscopy density. It remains an open question whether this local mismatch was caused by displacement of NLS-2×GFP by other cargoes and/or nucleoporins². Because our import reactions were carried out with cytosolic supernatant, other transport events involving (unlabelled) cargo, such as the export of ribosomal subunits and RNAs, are likely to proceed simultaneously with the import of the labelled cargo. In earlier studies, nucleoplasmin¹⁵ and messenger ribonucleoproteins¹⁶ caught in transport were both localized to the very centre of the central channel in individual NPCs. Three further observations can be derived from the cargo probability density. (1) The increased intensity at the cytoplasmic side in the area rich with cytoplasmic filaments suggests that these filaments supply initial docking sites for cargo complexes, as proposed earlier¹⁷. Although the cytoplasmic filaments are dispensable for nuclear import¹⁸, they might increase the effective docking surface and possibly the residence time for import complexes at the cytoplasmic entry of the pore¹⁹ and thereby speed up the (overall) translocation. (2) The gold-labelled cargoes we observed in the nuclear basket region were, in contrast to the cytoplasmic and central channel region, evenly distributed and without local enrichments, and therefore made only a minor contribution to the computed probability cloud. The lack of cargo density in the nuclear basket region can be

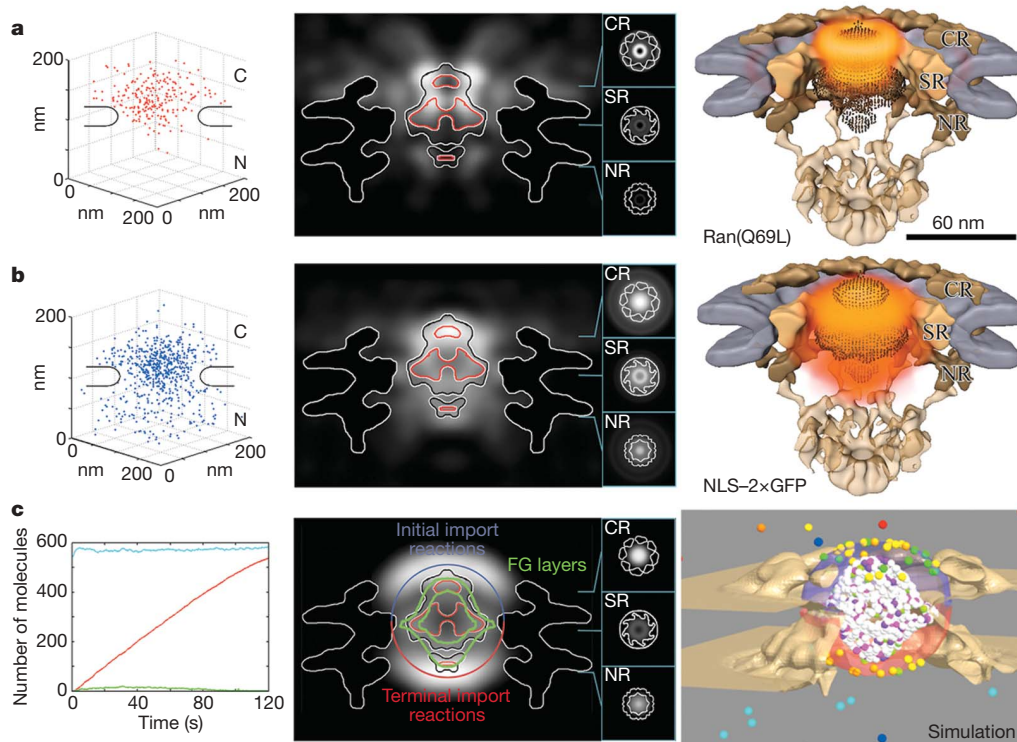


Figure 3 | Visualization of single molecules during nuclear import: experimental data and simulations. **a**, Gold-labelled Ran(Q69L)-GTP. Left: three-dimensional plot of the localization of Ran(Q69L)-GTP at the nuclear pore in the tomograms. Nuclear membranes are indicated on the sides. Middle: central slice along the nucleocytoplasmic axis of the (rotationally averaged) three-dimensional probability density map, superimposed onto the NPC structure. The three main electron-dense moieties of the central plug, in plane with the cytoplasmic (CR), spoke (SR) and nuclear rings (NR), are indicated by red lines and are shown as cross-sections in the insets. Right: three-dimensional probability distribution of Ran(Q69L)-GTP (orange clouds, brighter colour indicates higher probability) superimposed onto the central plug, which is shown as a dotted texture (brown). **b**, Gold-labelled classical import cargo NLS-2×GFP. Left, middle and right panels as for panel **a**. **c**, Computer simulations of nuclear import. Left: time courses of

translocated substrate molecules (red), cargo (green) and RanGTP (cyan). Middle: central slice along the nucleocytoplasmic axis of the (rotationally averaged) three-dimensional probability density map of cargo, superimposed onto the NPC structure. Central plug as in the middle panels of **a** and **b**. In addition, cytoplasmic (blue), nuclear (red) and phenylalanine-glycine (FG) effector surfaces (green) are indicated. Right: surface-rendered cut-away view of a simulation 20 s after initialization. Small spheres represent individual molecules (or complexes). Substrate, red; cargo, green; importin- α , orange; importin- β , yellow; RanGDP, bright cyan; RanGTP, dark cyan; Cas-importin- α -RanGTP, pink; importin- β -RanGTP, purple; cargo complexes bound to phenylalanine-glycine sites, bright green; unoccupied phenylalanine-glycine sites, white. The NPC structure and membranes are shown in dark yellow, and the cytoplasmic (blue) and nuclear effector surfaces (red) are represented as half spheres.

explained either by a cargo release directly from the central channel, or by a mobile terminal cargo complex binding site². (3) A gradient of binding sites with increasing affinity along the transport direction²⁰ would result in an increase in the probability density along the nucleocytoplasmic axis towards the nucleoplasm. We did not observe such a pattern in our experiments, although the intensity was higher at the exit of the central channel than within the central channel.

The GTP-hydrolysis of Ran at the cytoplasmic side of the NPC is the triggering event for the disassembly of export complexes²¹. In a control experiment (Fig. 3a), we mapped the positions of gold-conjugated Ran(Q69L)-GTP particles (127 labelled NPCs, 234 gold particles). This active site variant of Ran is unable to hydrolyse GTP and consequently can neither bind its import receptor NTF2 nor translocate into the nucleus in the conventional manner. It does interact with Ran-binding domains of the cytoplasmic filaments and is therefore expected to be localized mainly at the cytoplasmic side of the NPC²². The three-dimensional probability density of Ran(Q69L)-GTP indeed shows the highest intensities close to the outer part of the CP/T, in plane with the cytoplasmic ring. Nevertheless, we detected a small but significant number of gold-conjugated Ran(Q69L)-GTP particles inside the central channel, suggesting that they may enter the central channel by passive diffusion, albeit not very efficiently.

To clarify which parameters have a substantial impact on the local probability density of cargo, and illuminate some of the currently unresolved aspects of nuclear import, we used single-molecule three-dimensional Monte Carlo simulations of classical nuclear import in the microenvironment of an individual NPC (the shape of which was derived from the surface of our NPC structure). These simulations were done using the Mcell software package²³. They tracked each molecule (or molecular complex) separately as it diffused through the pore and reacted with other molecules.

The three main nuclear import steps—the initial formation and docking of a cargo complex to the central channel, its interaction with the phenylalanine-glycine meshwork during the main translocation, and a terminal cargo release event²⁴—were modelled in detail (Supplementary Table 1 and Supplementary Fig. 5). Essentially, there were only three parameters with undetermined values (see Supplementary Information). The values of other parameters—concentrations, diffusion constants, the permeabilities of the NPCs for diffusible molecules—as well as reaction constants (we modelled more than 50 reactions) were based on experimental data whenever possible. Some of them were adapted from earlier computer modelling^{25–27} that did not take into account single molecules, the actual structure of the NPC, or the membrane to NPC surface ratio that ultimately determines the likelihood for a molecule to encounter the central channel. In our model, the relevant chemical reactions (Supplementary Fig. 5) are considered to occur at defined locations, namely the cargo complex formation and release at the entrance and exit of the central channel, and the interactions with the phenylalanine-glycine meshwork in between (effector surfaces shown in Fig. 3c). The output of our simulations provided the position of each molecule at each time point, and consequently, the three-dimensional distribution of cargo that was directly compared with the experimentally determined positions.

The agreement of the simulations with the experimental data turned out to depend critically on two parameter choices. First, as two NLS-2×GFP molecules are, on average, conjugated to each gold bead, one (monomolecular import) or two (bimolecular import) NLS sequences can be occupied by importin heterodimers during translocation. The bimolecular reaction is kinetically slower, causing a local increase of the probability density at the cytoplasmic face. Second, two different terminal cargo release rates are available in the literature: the (fast release) rate used in earlier simulations²⁷, and the experimentally determined (slow release) rate for Nup50 (ref. 28), which would cause a local increase of the probability density at the nuclear face.

Two out of six simulation scenarios produced probability densities that satisfactorily fitted the experimental data (see Supplementary Table 2 for a quantitative assessment). First, if the fast cargo release rate is used, a monomolecular cargo assembly reaction is necessary to obtain consistent intensities (Supplementary Fig. 6). Second, if a slow cargo release rate is assumed, at least partially bimolecular cargo assembly must be used (Fig. 3c). Whereas the latter case produces a better match (Supplementary Table 2), it is characterized by a slower flux rate (Supplementary Fig. 6), because at high substrate concentrations the importin concentration becomes rate limiting, resulting in a relatively slow initial event.

The selective phase model predicts that importins compensate for surface charges of substrates to allow the passage through a hydrophobic permeability barrier in the central channel, which is formed by a three-dimensional meshwork of phenylalanine-glycine-rich repeats with hydrogel-like properties²⁹. Consequently, a high surface occupancy by importin- α/β heterodimers would result in a more effective transport of a cargo. Under conditions of excess substrate, one importin heterodimer may possibly tether a substrate to the phenylalanine-glycine meshwork, but the penetration of the meshwork would require the binding of a second importin heterodimer. The 'virtual gating' model¹⁹ does not rely on a different chemical environment but on the affinity of cargo complexes to phenylalanine-glycine repeats. Therefore, the selective phase model is consistent with partially bimolecular import, whereas the virtual gating model is more consistent with monomolecular import. Recent findings suggest that both principles are involved in nuclear transport³⁰.

We have shown that compensating for deviations from perfect symmetry is necessary to increase the attainable resolution. Our analysis has led to the identification of novel structural features of the NPC. To understand fully the NPC architecture, high-resolution structures of nucleoporins or subcomplexes have to be fitted into the complete structure. Furthermore, we were able to visualize the classical import route in three dimensions and to provide clear experimental evidence suggesting that the electron optical density of the CP/T correlates with cargo. Classical import complexes are concentrated in the regions of the CP/T located in plane with the cytoplasmic and nuclear rings on entry into and release from the central channel. The ratios between the respective cargo probability intensities at the entrance, at the exit and within the central channel point to a slow initial event under conditions of excess substrate. For a further understanding of the transport mechanism and the nature of the CP/T, the three-dimensional localization of cargoes of other transport pathways, as well as transport factors and receptors, is needed.

METHODS SUMMARY

Dictyostelium discoideum cells were grown in AX2 medium and lysed by passing them through a 5 μ m polycarbonate filter. Nuclei were enriched by centrifugation and, in the case of the cargo-tracing experiments, incubated in the presence of cytosolic supernatant and gold-labelled Ran(Q69L) or NLS-2×GFP, respectively. Afterwards the nuclei were pipetted onto lacy carbon grids and rapidly frozen in liquid ethane. Tilt series were collected with a Phillips CM 300 FEG or FEI Polara transmission electron microscope, typically covering an angular range from -63° to 63° and sampled with $1.5-2^\circ$ tilt increments. Tomographic reconstructions were calculated by weighted back-projection and single-particle alignments were performed using 'missing-wedge'-weighted correlation averaging. During the structural refinement the eight asymmetric units of all single particles were aligned independently; resolution tests were performed by Fourier-shell correlation using the 0.5 criterion. Gold particles were localized in the aligned subvolumes and their positions were used to compute three-dimensional probability distributions of Ran(Q69L) or NLS-2×GFP at the nuclear pore. Single-molecule Monte Carlo simulations of classical nuclear import were done with the Mcell software. The cryo-electron microscopy map of the *Dictyostelium* nuclear pore served as a framework; diffusion coefficients, concentrations of the relevant molecules, kinetic constants and reaction schemes were based on published experimental data and computer simulations.

Detailed protocols, sample preparations, electron microscopy techniques, and image processing and simulation procedures are available in the Supplementary Information.

Received 4 June; accepted 17 August 2007.

Published online 12 September 2007.

1. Fahrenkrog, B., Koser, J. & Aebi, U. The nuclear pore complex: a jack of all trades. *Trends Biochem. Sci.* **29**, 175–182 (2004).
2. Fahrenkrog, B. & Aebi, U. The nuclear pore complex: nucleocytoplasmic transport and beyond. *Nature Rev. Mol. Cell Biol.* **4**, 757–766 (2003).
3. Lucic, V., Forster, F. & Baumeister, W. Structural studies by electron tomography: from cells to molecules. *Annu. Rev. Biochem.* **74**, 833–865 (2005).
4. Beck, M. *et al.* Nuclear pore complex structure and dynamics revealed by cryoelectron tomography. *Science* **306**, 1387–1390 (2004).
5. Akey, C. W. Structural plasticity of the nuclear pore complex. *J. Mol. Biol.* **248**, 273–293 (1995).
6. Hinshaw, J. E. & Milligan, R. A. Nuclear pore complexes exceeding eightfold rotational symmetry. *J. Struct. Biol.* **141**, 259–268 (2003).
7. Saxton, W. O. & Baumeister, W. The correlation averaging of a regularly arranged bacterial cell envelope protein. *J. Microsc.* **127**, 127–138 (1982).
8. Saxton, W. O., Durr, R. & Baumeister, W. From lattice distortion to molecular distortion—characterizing and exploiting crystal deformation. *Ultramicroscopy* **46**, 287–306 (1992).
9. Melcak, I., Hoelz, A. & Blobel, G. Structure of Nup58/45 suggests flexible nuclear pore diameter by intermolecular sliding. *Science* **315**, 1729–1732 (2007).
10. Devos, D. *et al.* Components of coated vesicles and nuclear pore complexes share a common molecular architecture. *PLoS Biol.* **2**, e380 (2004).
11. Drin, G. *et al.* A general amphipathic α -helical motif for sensing membrane curvature. *Nature Struct. Mol. Biol.* **14**, 138–146 (2007).
12. Stoffler, D. *et al.* Cryo-electron tomography provides novel insights into nuclear pore architecture: implications for nucleocytoplasmic transport. *J. Mol. Biol.* **328**, 119–130 (2003).
13. King, M. C., Lusk, C. P. & Blobel, G. Karyopherin-mediated import of integral inner nuclear membrane proteins. *Nature* **442**, 1003–1007 (2006).
14. Yang, W., Gelles, J. & Musser, S. M. Imaging of single-molecule translocation through nuclear pore complexes. *Proc. Natl Acad. Sci. USA* **101**, 12887–12892 (2004).
15. Rutherford, S. A., Goldberg, M. W. & Allen, T. D. Three-dimensional visualization of the route of protein import: the role of nuclear pore complex substructures. *Exp. Cell Res.* **232**, 146–160 (1997).
16. Kiseleva, E., Goldberg, M. W., Allen, T. D. & Akey, C. W. Active nuclear pore complexes in *Chironomus*: visualization of transporter configurations related to mRNP export. *J. Cell Sci.* **111**, 223–236 (1998).
17. Pante, N. & Aebi, U. Sequential binding of import ligands to distinct nucleopore regions during their nuclear import. *Science* **273**, 1729–1732 (1996).
18. Walther, T. C. *et al.* The cytoplasmic filaments of the nuclear pore complex are dispensable for selective nuclear protein import. *J. Cell Biol.* **158**, 63–77 (2002).
19. Rout, M. P., Aitchison, J. D., Magnasco, M. O. & Chait, B. T. Virtual gating and nuclear transport: the hole picture. *Trends Cell Biol.* **13**, 622–628 (2003).
20. Ben-Efraim, I. & Gerace, L. Gradient of increasing affinity of importin beta for nucleoporins along the pathway of nuclear import. *J. Cell Biol.* **152**, 411–417 (2001).
21. Matunis, M. J., Coutavas, E. & Blobel, G. A novel ubiquitin-like modification modulates the partitioning of the Ran-GTPase-activating protein RanGAP1 between the cytosol and the nuclear pore complex. *J. Cell Biol.* **135**, 1457–1470 (1996).
22. Wu, J., Matunis, M. J., Kraemer, D., Blobel, G. & Coutavas, E. Nup358, a cytoplasmically exposed nucleoporin with peptide repeats, Ran-GTP binding sites, zinc fingers, a cyclophilin A homologous domain, and a leucine-rich region. *J. Biol. Chem.* **270**, 14209–14213 (1995).
23. Coggan, J. S. *et al.* Evidence for ectopic neurotransmission at a neuronal synapse. *Science* **309**, 446–451 (2005).
24. Becskei, A. & Mattaj, J. W. Quantitative models of nuclear transport. *Curr. Opin. Cell Biol.* **17**, 27–34 (2005).
25. Smith, A. E., Slepchenko, B. M., Schaff, J. C., Loew, L. M. & Macara, I. G. Systems analysis of Ran transport. *Science* **295**, 488–491 (2002).
26. Gorlich, D., Seewald, M. J. & Ribbeck, K. Characterization of Ran-driven cargo transport and the RanGTPase system by kinetic measurements and computer simulation. *EMBO J.* **22**, 1088–1100 (2003).
27. Riddick, G. & Macara, I. G. A systems analysis of importin- α - β mediated nuclear protein import. *J. Cell Biol.* **168**, 1027–1038 (2005).
28. Matsuura, Y. & Stewart, M. Nup50/Npap60 function in nuclear protein import complex disassembly and importin recycling. *EMBO J.* **24**, 3681–3689 (2005).
29. Frey, S., Richter, R. P. & Gorlich, D. FG-rich repeats of nuclear pore proteins form a three-dimensional meshwork with hydrogel-like properties. *Science* **314**, 815–817 (2006).
30. Patel, S. S., Belmont, B. J., Sante, J. M. & Rexach, M. F. Natively unfolded nucleoporins gate protein diffusion across the nuclear pore complex. *Cell* **129**, 83–96 (2007).

Supplementary Information is linked to the online version of the paper at www.nature.com/nature.

Acknowledgements We thank F. Melchior for the Ran(Q69L) protein, S. Musser for the NLS-2×GFP plasmid, G. Gerisch and J. Glavy for valuable discussions, and A. Leis for critical reading of the manuscript. This work was supported in part by the European Union 3DEM Network of Excellence.

Author Information The structure has been deposited at the Macromolecular Structure database (EBI) under accession code EMD-1394. Reprints and permissions information is available at www.nature.com/reprints. Correspondence and requests for materials should be addressed to W.B. (baumeister@biochem.mpg.de) or O.M. (omedalia@bgu.ac.il).